Title

Comparison of decoding resolution of standard and high-density electrocorticogram electrodes.

Journal

Journal of neural engineering, 13(2)

ISSN

1741-2560

Authors

Wang, Po T
King, Christine E
McCrimmon, Colin M
et al.

Publication Date

2016-04-01

DOI

10.1088/1741-2560/13/2/026016

Peer reviewed

HHS Public Access

Author manuscript

J Neural Eng. Author manuscript; available in PMC 2019 May 09.

Published in final edited form as:

J Neural Eng. 2016 April ; 13(2): 026016. doi:10.1088/1741-2560/13/2/026016.

Comparison of decoding resolution of standard and high-density electrocorticogram electrodes

Po T. Wang[1], **Christine E. King**[2], **Colin M. McCrimmon**[1], **Jack J. Lin**[3], **Mona Sazgar**[3], **Frank P.K. Hsu**[4], **Susan J. Shaw**[5,6,7], **David E. Millet**[6,7,8], **Luis A. Chui**[3], **Charles Y. Liu**[6,7,9,10], **An H. Do**[3,*], and **Zoran Nenadic**[1,11,*]

[1.] Department of Biomedical Engineering, University of California, Irvine, CA 92697

[2.] Department of Neurology, University of California, Los Angeles, CA 90095

[3.] Department of Neurology, University of California, Irvine, CA 92697

[4.] Department of Neurosurgery, University of California, Irvine, CA 92697

[5.] Department of Neurology, Rancho Los Amigos National Rehabilitation Center, Downey, CA 90242

[6.] Department of Neurology, University of Southern California, Los Angeles, CA 90089

[7.] Neurorestoration Center, University of Southern California, Los Angeles, CA 90089

[8.] Hoag Hospital, Newport Beach, CA 92663

[9.] Department of Neurosurgery, Rancho Los Amigos National Rehabilitation Center, Downey, CA 90242

[10.] Department of Neurosurgery, University of Southern California, Los Angeles, CA 90089

[11.] Department of Electrical Engineering and Computer Science, University of California, Irvine, CA 92697

Abstract

Objective—Electrocorticography (ECoG)-based brain-computer interface (BCI) is a promising platform for controlling arm prostheses. To restore functional independence, an ECoG-based BCI must be able to control arm prostheses along at least six degrees-of-freedom (DOFs). Prior studies suggest that standard ECoG grids may be insufficient to decode multi-DOF arm movements. This study compared the ability of standard and high-density (HD) ECoG grids to decode the presence/absence of six elementary arm movements and the type of movement performed.

Approach—Three subjects implanted with standard grids (4 mm diameter, 10 mm spacing) and three with HD grids (2 mm diameter, 4 mm spacing) had ECoG signals recorded while performing the following movements: (1) pincer grasp/release, (2) wrist flexion/extension, (3) pronation/supination, (4) elbow flexion/extension, (5) shoulder internal/external rotation, and (6) shoulder forward flexion/extension. Data from the primary motor cortex were used to train a state decoder

[*]Communicating authors (and@uci.edu, znenadic@uci.edu).

to detect the presence/absence of movement, and a six-class decoder to distinguish between these movements.

Main Results—The average performances of the state decoders trained on HD ECoG data were superior ($p = 3.05 \times 10^{-5}$) to those of their standard grid counterparts across all combinations of the μ, β, low-γ, and high-γ frequency bands. The average best decoding error for HD grids was 2.6%, compared to 8.5% of standard grids. The movement decoders trained on HD ECoG data were superior ($p = 3.05 \times 10^{-5}$) to those based on standard ECoG across all band combinations. The average best decoding errors of 11.9% and 33.1% were obtained for HD and standard grids, respectively. These improvements can be attributed to higher electrode density and signal quality of HD grids.

Significance—Commonly-used ECoG grids are inadequate for multi-DOF BCI arm prostheses. The significant decoding performance gains achieved by HD grids may eventually lead to independence-restoring BCI control of arm prosthesis.

1 Introduction

Electrocorticogram (ECoG) has been increasingly studied as a neuronal signal acquisition modality for brain-computer interface (BCI) applications. A large majority of ECoG-based BCI studies to date has focused on decoding the kinematic parameters of upper extremity movements, with the ultimate goal of interfacing these systems with upper extremity prostheses. Examples include decoding the trajectories of individual fingers [1, 2, 3], elbow and hand [4], as well as the onset and direction of reaching movements [5, 6]. However, reaching, grasping, and finger movements alone are insufficient for restoring independence to those with upper extremity paralysis due to conditions such as subcortical stroke or spinal cord injury (SCI). For example, the ability to perform daily activities such as grooming, dressing, toileting, bathing and bed/chair transferring is essential for achieving functional independence [7]. Analyses have shown that performing these tasks requires an arm prosthesis with at least six degrees of freedom (DOFs) [8]. In summary, the ability to decode arm movements beyond reaching and grasping is paramount for attaining meaningful, independence-restoring BCI upper extremity prosthesis control.

An ECoG-based BCI system capable of achieving six-DOF upper extremity prosthesis control must be able to determine when and where to move along individual DOFs. A bare-minimum strategy to accomplish this goal is to design a decoding algorithm that can answer the following questions: 1. Is there a movement? 2. If so, which DOF(s) is (are) involved? 3. What is the movement direction (e.g. flexion or extension) of the DOF(s) involved? The authors' preliminary studies suggest that correctly answering these questions may be difficult with signals from standard ECoG electrode grids. Namely, the ECoG signals most informative of six elementary arm movements were found to be confined to approximately three primary motor cortex (M1) electrodes [9]. This is not surprising, given the size of the arm motor representation area [10] and the relatively limited spatial resolution of standard ECoG grids, with a typical electrode diameter of 4 mm and an inter-electrode distance of 10 mm. Consequently, movements, especially those with adjacent M1 representations, were classified with a significant degree of confusion [11]. For example, pincer grasp/release was often misclassified as wrist flexion/extension, and elbow flexion/extension as shoulder

flexion/extension. Based on these observations, it can be hypothesized that increasing the density of ECoG electrodes may yield signals that better resolve elementary upper extremity movements, which may lead to more accurate multi-DOF BCI control of arm prostheses.

Historically, ECoG grids of increased density have been developed to improve clinicians' ability to localize epilepsy foci [12]. They were subsequently adopted for research purposes such as BCI applications, with the goal of improving BCI performances. For example, microwire ECoG grids (diameter: 40–75 μm, inter-electrode distance: 1 mm) have been used to study the encoding of finger movements in monkeys [13], as well as of wrist flexion/extension and the direction of arm movements in humans [14, 15]. Similarly, high-density (HD) ECoG grids (diameter: 2 mm, inter-electrode distance: 4 mm) have been used to classify individual finger movements [16, 17], decode grasping force [18], and achieve three-dimensional (3D) control of an arm prosthesis end-effector [19].

To the best of the authors' knowledge, there have been no formal, systematic comparisons between the decoding resolution of standard and HD ECoG grids for BCI applications. Therefore, the presumed advantage of HD grids in BCI applications remains mostly anecdotal [19]. In addition, with the exception of the authors' preliminary studies [9, 11], there have not been any ECoG studies that examined the ability to decode movements at the six principal upper extremity DOFs. Motivated by this knowledge gap, the present study collected ECoG data underlying six elementary upper extremity movements from subjects implanted with standard or HD ECoG grids. Based on these data, decoders were designed to answer questions 1 and 2 above. The performances of the decoders trained on standard and HD signals were then characterized, compared and discussed.

2 Methods

2.1 Overview

Subjects with standard or HD grids implanted subdurally over M1 performed a series of six elementary upper extremity movements while their ECoG and arm trajectories were recorded. The signals were then separated into μ (8–13 Hz), β (13–30 Hz), low-γ (30–50 Hz), and high-γ (80–160 Hz) frequency bands, and combined to obtain: 1. State decoder—a binary classifier with the goal of detecting the presence/absence of elementary arm movements; 2. Movement decoder—a six-class classifier to determine which elementary movement was performed. The decoding accuracy across four individual frequency bands and all possible band combinations was estimated using cross-validation. Based on these results, the ability to detect when and which elementary arm movements occurred was assessed for both standard and HD ECoG signals.

2.2 Data Collection

The study was approved by the Institutional Review Boards of the University of California, Irvine and the Rancho Los Amigos National Rehabilitation Center. Subjects were recruited from a patient population undergoing epilepsy surgery evaluation. They were subdurally implanted with either standard or HD electrode grids (Integra LifeSciences, Plainsboro, NJ). Standard grids consisted of arrays of 4-mm-diameter platinum electrodes, spaced 10 mm

apart. HD grids consisted of 2-mm-diameter platinum electrodes that were 4 mm apart. Only patients with grids covering the upper extremity M1 area were recruited for the study. Using a dedicated cable (Plastics One, Roanoke, VA), each ECoG signal was split at the headbox, with one copy used clinically and the other used for the present study. Up to 64 channels of ECoG data were recorded with a pair of linked NeXus-32 bioamplifiers (Mind Media, Roermond-Herten, The Netherlands). Electrodes with excessive noise were unplugged from the amplifier prior to recording. Signals were acquired in a common average reference mode at a rate of 2048 Hz. The bioamplifiers had a built-in low-pass filter with a roll-off frequency of 0.27 times the sampling rate (i.e. 553 Hz).

The subjects performed the following six elementary movements with the arm contralateral to their implant: 1. pincer grasp/release (PG), 2. wrist flexion/extension (W), 3. forearm pronation/supination (PS), 4. elbow flexion/extension (E), 5. shoulder internal/external rotation (SR), and 6. shoulder forward flexion/extension (SFE). The trajectories of PG and W movements were measured by a custom-made flexible electrogoniometer [20], and those of the remaining movements were measured by a gyroscope (Wii Motion Plus, Nintendo, Kyoto, Japan). These signals were acquired using an integrated microcontroller unit (Arduino, Smart Projects, Turin, Italy). The bioamplifier and microcontroller unit were synchronized using a common pulse train sent to both acquisition systems. For each DOF, subjects performed 4 sets of 25 continuous movement repetitions, with each set intervened by a 20–30 s rest (idling) period (see Fig. 1).

2.3 M1 Localization and Power Modulation Analysis

To ensure that the results are based on motor signals (as opposed sensory feedback), the primary focus of the study was decoding from M1 electrodes. For this purpose, the electrodes were first localized through co-registration of the magnetic resonance imaging (MRI) and computed tomography (CT) scans of the head using the technique described in [21]. Once the images were co-registered, M1 was anatomically defined as the area between the central and pre-central sulci, and electrodes overlying this area were identified. Since epilepsy may cause functional deviation from classical anatomy [22, 23], additional tests were performed to affirm that the anatomical M1 area was functionally involved in upper extremity movements. Specifically, for each movement type and each channel, a contrast index (CI) was first calculated as the difference in the high-γ band power during movement and idling periods (see below for details). The restriction of the CI to this band was motivated by the fact that the high-γ frequencies represent the main components of the cortical activity underlying arm movements [1, 24, 25, 26, 27, 28]. The anatomical M1 channels were deemed functionally relevant if they satisfied the following condition:

$$\mathrm{CI}_{\mathrm{M1}} > \overline{\mathrm{CI}}_{\mathrm{non-M1}} + 2\sigma_{\mathrm{non-M1}} \quad (1)$$

where $\mathrm{CI}_{\mathrm{M1}}$ is the CI value of each anatomical M1 channel, and $\overline{\mathrm{CI}}_{\mathrm{non-M1}}$ and $\sigma_{\mathrm{non\text{-}M1}}$ are respectively the mean and standard deviation of the CI for non-M1 channels. The presence of one or more functionally-relevant M1 channels was used as a criterion to confirm the alignment of anatomical and functional M1 areas.

To calculate the CI for each type of elementary movement, the ECoG and motion sensor data were first aligned using the synchronization pulse train (see Section 2.2). The epochs of ECoG signals underlying movement periods were then segmented into individual flexion and extension intervals. Similarly, the epochs of ECoG signals underlying idling periods were segmented into "intervals" with an average duration matching those of flexion and extension intervals. Subsequently, the instantaneous high-γ band power [9] was calculated as:

$$P_{\gamma}(t) = f\left(x^2(t)\right) \quad (2)$$

where x is the bandpass (80–160 Hz) ECoG signal at each channel and $f(\cdot)$ is a 2.5 Hz low-pass envelope filter. The instantaneous powers were then normalized [29], so that the median and median absolute deviation (MAD) of P_{γ} during idling periods were 0 and 1, respectively. The standardized powers were then time-averaged over the duration of flexion, extension and idling intervals. Finally, the CI was defined as the absolute value of the Welch's t-statistic [30]:

$$\mathrm{CI} = \frac{\left|\mu_M - \mu_I\right|}{\sqrt{\frac{\sigma_M^2}{n_M} + \frac{\sigma_I^2}{n_I}}} \quad (3)$$

where μ_M and μ_I are respectively the standardized, time-averaged P_{γ}, averaged over movement and idling intervals, σ are their corresponding standard deviations, and n_M and n_I are the number of movement and idling intervals, respectively. Note that $n_M = n_F + n_E$, where n_F (n_E) is the number of flexion (extension) intervals.

An additional analysis was performed to investigate the time courses of P_{γ} for the most functionally-relevant M1 channels, as well as the primary somatosensory cortex (S1) channels. Namely, for an electrode recording primarily motor signals, the build-up of P_{γ} is expected to precede that of a sensory electrode. Therefore, the onsets of the four movement periods (Fig. 1) were defined as the instances at which the movement velocity exceeded 5°/s, and the data across the four idle-to-move transition periods were aligned correspondingly. The M1 and S1 channels with the highest CI value were then identified, and their respective normalized P_{γ} were averaged over the four transition periods and compared.

2.4 Decoder Design and Testing

The ECoG epochs underlying both idling and movement were segmented into 750-ms-long non-overlapping trials, and each ECoG trial was transformed into the frequency domain using the Fast Fourier Transform (FFT). Each trial's power spectral density (PSD) was then integrated over the μ, β, low-γ, and high-γ frequency bands. Note that these frequencies were selected because they are known to modulate with upper extremity movements [9, 26, 31]. Finally, the disparity in power levels, especially between the μ and high-γ bands, was reduced by taking the logarithm of the integrated power spectral densities.

2.4.1 State Decoder—The trials of spatio-spectral ECoG data underlying all six movement types were grouped into a single *Move* class. Similarly, the trials corresponding to idling epochs across all movement types were grouped into a single *Idle* class. Features were then extracted from these high-dimensional spatio-spectral data by using a combination of classwise principal component analysis (CPCA) [32] and approximate information discriminant analysis (AIDA) [33]. More specifically, one-dimensional (1D) spatio-spectral features were extracted by:

$$f = T_A \Phi_C(d) \quad (4)$$

where $f \in \mathbb{R}$ is the feature, $\mathrm{d} \in \mathbb{R}^{BC\times 1}$ is a single-trial spatio-spectral ECoG matrix reshaped in a vector form (*B*-the number of frequency bands, *C*-the number of channels), $\mathbf{\Phi}_C : \mathbb{R}^{BC\times 1} \rightarrow \mathbb{R}^{m\times 1}$ is a piecewise linear mapping from the data space into the *m*-dimensional CPCA-subspace, and $\mathbf{T}_A \in \mathbb{R}^{1\times m}$ is an AIDA transformation matrix. This approach, whose detailed description can be found in [32, 33], enhances class separability by maximizing an information-theoretic class separability criterion [34]. Its distinct characteristic is that it can handle high-dimensional data under small sample size conditions (data dimension > sample size), without resorting to simplifying assumptions [32]. In addition, the resulting features depend on data nonlinearly, yet the method retains the computational simplicity of linear feature extraction techniques.

In the second stage, a binary classifier was trained in the feature domain to distinguish between *Idle* and *Move* states. To this end, a Bayesian classifier was designed as follows:

$$f^\star \in \mathcal{S}_{i^\circ} \text{ where } i^\circ = \arg\max_{i=\{1,2\}} P\left(\mathcal{S}_i \middle| f^\star\right) \quad (5)$$

with $P\left(\mathcal{S}_i | f^\star\right)$ being the posterior probability of state $\mathcal{S}_i$ (*Idle:* $i = 1$, *Move:* $i = 2$) given the observed feature f^*. The posterior probabilities were calculated using the Bayes rule [35, p. 24], after assuming that the class-conditional distributions of features were Gaussian.

The accuracy of the feature extraction and classification models was then estimated by performing 10 runs of stratified 10-fold cross-validation [36] as follows:

1. The spatio-spectral dataset was randomly divided into 10 non-overlapping folds of equal size while preserving the relative frequencies of *Idle* and *Move* classes.
2. One of the folds was designated as test data and the remaining nine folds were combined into a single training dataset.
3. From the training set, the feature extraction transform (4) was estimated. The training data were transformed into the feature domain and the parameters of the classifier were estimated. The test data were transformed in the same manner, and their class labels were determined according to (5). The number of misclassified cases was logged.

4. Steps 2 and 3 were repeated until all the folds were exhausted. The classification error was calculated as the total number of misclassified cases divided by the total number of test cases.

5. The above steps were repeated 10 times and the final classification error was evaluated as the average over 10 runs.

To investigate how individual frequency bands contributed to the decoder performance, the above procedure was repeated using each of the frequency bands individually, as well as all possible two-band and three-band combinations.

2.4.2 Movement Decoder—Similar to Section 2.4.1, the trials of spatio-spectral ECoG data underlying different movement types were grouped into six classes. Feature extraction maps were then found using CPCA [32] followed by AIDA [33], with the goal of maximizing class separability [34]. Formally, a model similar to (4) was adopted, albeit with a higher dimension of the feature space (3D vs. 1D). The increase in the feature space dimension is not surprising given the increase in the number of classes from two to six. According to the Bayesian decision theory [37, p.444], the optimal dimension of the feature space would be five (one less than the number of classes), though the extraction of Bayes-optimal features would require infinite number of samples. For finitely sampled data, the feature space dimension may depart from the theoretical optimum. In addition, the performance of the classifiers described below did not improve substantially by increasing the dimension of feature space beyond three.

Subsequently, a six-class linear Bayesian classifier was trained in the 3D feature domain:

$$f^{\star} \in \mathcal{M}_{i^{\circ}} \text{where} i^{\circ} = \arg \max_{1 \le i \le 6} P\left(\mathcal{M}_i \middle| f^{\star}\right) \quad (6)$$

and $P\left(\mathcal{M}_i | f^{\star}\right)$ is the posterior probability of movement type $\mathcal{M}_i$ ($i = 1, 2, \cdots, 6$), given the observed feature $f^{\star}$. These posterior probabilities were evaluated in a manner similar to Section 2.4.1. Likewise, the accuracy of the feature extraction and classification methods was estimated by performing 10 runs of stratified 10-fold cross-validation. Finally, the calculations were repeated using individual frequency bands and their combinations.

2.5 Control Analysis

To control for factors other than a grid density, the HD grids were spatially sub-sampled to mimic the electrode density of standard grids. Therefore, every other electrode row/column was removed from the HD grids, and the signals from the remaining M1 electrodes were used for analysis as described above. Note that this effectively created grids with electrodes 8 mm apart, thus resembling standard grids with the 10 mm inter-electrode distance. Since spatial sub-sampling can be achieved by removing odd/even rows and odd/even columns, the decoding results corresponding to spatially sub-sampled HD grids were obtained by averaging over these four combinations. In addition, to account for a difference in the number of M1 electrodes for standard and HD grids, the decoding analysis was repeated while matching the number of standard and HD M1 electrodes. Finally, the whole-grid

decoding was performed with the goal of investigating the extent to which information outside of the anatomical M1 area contributed to the state and movement decoding.

3 Results

Six subjects undergoing epilepsy surgery evaluation provided their informed consent to participate in the study. Three subjects were implanted with standard grids and three were implanted with HD grids. Their demographic data, implantation area, and the type of grid are presented in Table 1. It should be noted that the implantation areas, grid types and the number of electrodes were determined by the clinical needs of individual patients, and were in no way influenced by the current study. Raw ECoG signals from each subject were inspected prior to analysis. With the exception of Subject 2, epileptiform activity was rare and sporadic throughout the study recordings. In Subject 2, epileptiform activity was observed in posterior-inferior parietal area every 3–5 s throughout the entire experiment (occurring evenly in idling and movement tasks). These signals were ultimately excluded from analysis as they were not in M1.

3.1 M1 Localization and Power Modulation Analysis

The electrodes were localized based on the MRI and CT scans of the head using the technique described in [21]. For Subjects 1 and 2, this was accomplished by co-registering the post-implantation CT and MRI scans. For Subjects 3, 5, and 6, post-implantation MRI scans were not available, therefore the pre-implantation MRI scans were used instead. For Subject 4, MRI was not performed due to the presence of MRI-incompatible metal in his body; thus the electrode localization was done based on the CT scan alone. The electrode locations in reference to the brain anatomy are shown in Fig. 2. Note that Subject 2 had left frontal porencephaly, likely caused by an intrauterine stroke.

The location of M1 was determined by first finding the superior frontal gyrus, followed by identification of the pre-central sulcus as the posterior border of the superior frontal gyrus. M1 was identified as the gyrus immediately posterior to the pre-central sulcus. Similarly, anatomical landmarks were used to identify the central sulcus. The locations of the pre-central and central sulci were then manually traced out (Fig. 2), and M1 electrodes were demarcated. Subsequently, S1 was identified as the gyrus immediately posterior to the central sulcus. The breakdown of the number of M1 channels across subjects is shown in Table 2. Not surprisingly, the HD grids had a higher number of M1 electrodes (average: 27.7) compared to the standard grids (average: 13.7). Based on the electrode density alone, this ratio is expected to exceed 4:1, however, HD grids were smaller, and so they covered proportionately smaller brain areas (Fig. 2).

For each channel and each movement type, the CI was calculated according to (3). Generally, the values of CI were elevated over the sensory-motor areas across all movement types and subjects. Note that this observation is consistent with a high-γ event-related synchronization [9], i.e. an increase in the γ band power elicited by movements, and its decrease caused by idling. Figs. 3 and 4 show representative CI maps for subjects with standard and HD grids, respectively. The remaining CI maps can be found in the Appendix (see Figs. A1–A4). The Appendix also provides an example of a movement-related power

modulation across multiple frequency bands (see Fig. A5). Note that the most salient features were event-related desynchronization in the μ and β bands, and event-related synchronization in the low-γ and high-γ bands.

Once the CIs were calculated, the criterion (1) was applied to identify functionally-relevant M1 channels, whose number varied across movement types, grid types, and subjects. The total number of functionally-relevant M1 channels, N_{fr}, is given in Table 2. Note that N_{fr} was on average higher in HD grids (8.7) than in standard grids (6.0). In addition, the average values of the contrast index, $\overline{CI}$, were higher in HD grids, and this was true for both M1 and non-M1 areas. Also note that $\overline{CI}$ was the highest in functionally-relevant M1 channels, followed by M1 channels and non-M1 channels. In conclusion, these results confirmed a general alignment of the functional and anatomical M1 areas.

Finally, for M1 and S1 channels with the highest CI value, the time courses of P_γ were analyzed as described in Section 2.3. As can be seen from Fig. A6 (Appendix), the movement-modulated build-up of the high-γ power was faster in M1 than in the S1 channels. This was true across all movement types and both grid types. In addition, the time courses of motor P_γ preceded those of their sensory counterparts by 86 ms and 38 ms for standard and HD grids, respectively (see Table A1 in the Appendix). Note that these values are within the physiologically plausible range of motor/sensory conduction times [38, 39]. In summary, this analysis indicated that M1 signals primarily encoded for motor intent, whereas those in S1 were primarily driven by sensory feedback.

3.2 State Decoder

3.2.1 Average Performances—The classification error of the state decoder (5) is presented in Fig. 5. While the results vary across subjects, grid types and frequency bands, the average classifier performance based on HD data, $\overline{HD}$, was uniformly (across all band combinations) superior to its standard data counterpart, $\overline{S}$. This was confirmed by performing a one-tailed sign test that suggested a significant difference between $\overline{HD}$ and $\overline{S}$ ($p = 3.05 \times 10^{-5}$). Upon averaging $\overline{S}$ and $\overline{HD}$ across all band combinations, it can be concluded that the use of HD grids reduced the decoding error from 13.5% to 7.3%, which corresponds to a relative error reduction of 46.7%.

3.2.2 Single-Band Performances—The minimum decoding errors across individual frequency bands (denoted by †) showed that no single band was superior. Namely, for standard grids, the most useful information was found in both β (Subjects 2 and 3) and high-γ (Subject 1) bands. For HD grids, the high-γ (Subjects 4 and 5) and μ (Subject 6) bands were found to be the most useful. By averaging results over subjects, the β and high-γ bands were the most useful for standard and HD grids, respectively (see columns $\overline{S}$ and $\overline{HD}$ in Fig. 5). Conversely, the low-γ band played the least significant role in both grid types.

3.2.3 Two-Band and Three-Band Combination Performances—In general, the decoding performance based on two-band or three-band combinations was higher if the combination included the high-γ band. For standard grids, including the high-γ band reduced the decoding error significantly (one-tailed rank-sum test, $p = 3.27 \times 10^{-2}$), with the

corresponding average errors of 13.3% and 11.5%. The performance gains were even more pronounced in HD grids, where the presence of the high-γ band reduced the average error from 9.3% to 3.2%. These differences were also statistically significant, as ascertained by a one-tailed rank-sum test ($p = 1.08 \times 10^{-5}$). On the other hand, the presence of the μ frequency band in any two-band or three-band combination tended to increase the average decoding error, but these differences were not statistically significant ($p > 0.05$). Similarly, the presence/absence of the β or low-γ band did not affect the decoding error in a statistically significant manner.

3.2.4 All-Band and Best Performances—The decoding error based on the combination of all four frequency bands coincided with the smalllest overall error (denoted by ‡) in Subjects 2, 3, and 5. Similarly, for Subjects 1, 4, and 6, the combination of all bands yielded errors that were very close to the overall minimum (within 1.5%). Note that for each subject, the best performances were always achieved in a band combination that contained the high-γ frequency band (see Fig. 5). By averaging the best overall performances across subjects, the decoding errors of 8.5% and 2.6% were obtained for standard and HD grids, respectively. Therefore, on average, the use of HD grids caused a 69.4% relative reduction in the minimum decoding error.

3.2.5 Control Analysis—The spatial sub-sampling of the HD grids resulted in a significant increase in the decoding error, $\overline{\mathrm{HD}}_{\mathrm{sub}}$, as ascertained by a one-tailed sign test ($p = 3.05 \times 10^{-5}$). Averaging $\overline{\mathrm{HD}}_{\mathrm{sub}}$ over all band combinations resulted in a decoding error of 10.9%, which represents a relative increase of 51.4% with respect to the average $\overline{\mathrm{HD}}$ error (7.2%). On the other hand, $\overline{\mathrm{HD}}_{\mathrm{sub}}$ remained generally smaller than $\overline{\mathrm{S}}$, especially when using three-band or four-band combinations. However, these differences were not statistically significant (sign test, $p = 5.92 \times 10^{-2}$). In summary, upon spatial sub-sampling, the decoding errors of the HD grids were significantly increased and approached those of the standard grids.

Since HD and standard grids had on average ~28 and ~14 M1 electrodes, respectively (see Table 2), additional decoding analysis was performed to control for the discrepancy in channel count. Specifically, the HD channels were ranked by the absolute value of feature extraction coefficients (4), and a subset of the top N_s ($N_s \geq 14$) channels was selected (such that their error was within a prespecified tolerance of the original error). An iterative search was then performed over $\binom{N_s}{14}$ combinations until the decoding performance of these 14 channels matched or exceeded that achieved with the full set of channels. The above procedure was performed using only the combination of all frequency bands. A comparison with the original decoding results (based on all M1 channels) is given in Table 3. As can be seen, the decoding errors based on the subset of 14 M1 channels were smaller than the original ones. Therefore, it can be concluded that the superior state decoding performance of HD grids was not caused by having more electrodes in M1.

To account for information outside of anatomical M1 areas, the state decoding analysis was repeated using all available electrodes (see Table 2). The results are presented in Fig. A7 in

the Appendix. Generally, the whole-grid decoding led to an improved performance across all band combinations (one-tailed sign test, $p = 3.05 \times 10^{-5}$ for Subjects 1, 2, 3 and 6, and $p = 4.88 \times 10^{-4}$ for Subject 5). A notable exception was Subject 4, whose performance generally worsened, but the change was not statistically significant. Upon averaging over all frequency band combinations, the relative error changes of −37.8%, −13.8%, −15.2%, −6.3%, −25.0%, and −24.5%, were observed for Subjects 1–6, respectively. Similar results were obtained by comparing the best performances (minimum errors), where the whole-grid decoding led to relative error changes of −37.5%, −14.7%, −17.6%, +50.0%, −28.9%, and −26.5%, for Subjects 1–6, respectively. These results indicate that the inclusion of non-M1 areas generally improved the decoding results. This conclusion is consistent with Figs. 3 and 4 and Figs. A1–A4 (Appendix), which indicate that most of the additional information came from S1. More importantly, upon utilizing all available channels, the advantage of HD over standard grids was retained. For example, by comparing $\overline{\text{S}}$ and $\overline{\text{HD}}$ (Fig. A7), it that be concluded that the use of HD grids reduced the average decoding error from 10.7% to 5.9%. This constitutes a relative error reduction of 44.9%—an improvement comparable to M1 decoding (cf. Section 3.2.1). Similarly, by averaging the best performances over subjects, HD grids reduced the decoding error from 6.6% to 2.0%. This represents a relative error reduction of 69.7%, and is in agreement with M1 decoding (cf. Section 3.2.4).

3.3 Movement Decoder

3.3.1 Average Performances—The classification error of the movement decoder (6), presented in Fig. 6, shows that the decoding performances based on HD data were nearly uniformly (across all subjects and band combinations) superior to their standard data counterparts. Consequently, the average performances $\overline{\text{HD}}$ were uniformly superior to $\overline{\text{S}}$, as confirmed by a right-tail sign test ($p = 3.05 \times 10^{-5}$). By averaging $\overline{\text{HD}}$ and $\overline{\text{S}}$ over all band combinations, it was found that the use of HD grids reduced the decoding error from 42.2% to 23.7%, which represents a relative error reduction of 43.8%.

3.3.2 Single-Band Performances—For individual bands, the decoding errors tended to monotonically decrease from low to high frequencies, and this was observed in both grid types. This suggests that the amount of useful information increased going from the μ band to the high-γ band.

3.3.3 Two-Band and Three-Band Combination Performances—The decoding errors achieved with two-band or three-band combinations were consistent with the above observations. Namely, for standard grids, the presence of the high-γ band significantly improved the performance (one-tailed rank-sum test, $p = 3.53 \times 10^{-4}$), with the average decoding error reduced from 46.1% to 35.7%. Similar to the state decoder (Section 3.2.3), the performance gains were even more apparent for HD grids, where the average decoding errors with and without γ band were 13.9% and 30.2%, respectively. These improvements were also statistically significant, as demonstrated by a one-tailed rank-sum test ($p = 4.37 \times 10^{-6}$). Conversely, the presence of the μ band resulted in an increase of the decoding error. This increase was not significant for standard grids and was significant for HD grids (one-tailed rank-sum test $p = 2.2 \times 10^{-2}$), with the average error increased from 16.6% to 23.0%.

As was the case with the state decoding, the presence/absence of the β or low-γ band in any two-band or three-band combination did not significantly affect the performance.

3.3.4 All-Band and Best Performances—The minimum decoding errors (marked by ‡) were achieved using the combination of β, low-γ and high-γ bands for Subjects 2, 3, and 4, and the combination of all bands for Subjects 1, 5, and 6. Similar to the state decoder, the performances based on all frequency bands were generally within 1.5% of the best overall performances. By averaging the best overall performances over subjects, the minimum decoding errors of 33.1% and 11.9% were respectively obtained for standard and HD grids. This represents a relative error reduction of 64.0%.

3.3.5 Control Analysis—Control analysis showed that upon spatial sub-sampling, the performance of the movement decoder, $\overline{\text{HD}}_{\text{sub}}$, deteriorated uniformly across all frequency band combinations (one-tailed sign test $p = 3.05 \times 10^{-5}$). When averaged over all band combinations, $\overline{\text{HD}}_{\text{sub}}$ yielded the decoding error of 40.1%, which represents a relative increase of 69.2% with respect to the average $\overline{\text{HD}}$ (23.7%). On the other hand, even though $\overline{\text{HD}}_{\text{sub}}$ was generally smaller than $\overline{\text{S}}$, especially for band combinations involving the high-γ frequency, these differences were not statistically significant (sign test, $p = 15.09 \times 10^{-2}$). In summary, spatial sub-sampling of the HD grids yielded decoding errors that approached those of the standard grids.

Additional analysis was performed to prove that the superior performance of the HD grids was not caused by them having a larger number of M1 channels. Following the procedure outlined in Section 3.2.5, a combinatorial search was performed to find a subset of 14 M1 channels whose performance matched or exceeded the original HD performances. The results are presented in Table 4. Since the decoding errors based on the subset of 14 M1 channels are smaller than those based on all M1 channels, it follows that HD grids did not outperform standard grids at the expense of having more M1 channels.

Analogous to Section 3.2.5, the movement decoding analysis was performed using all available electrodes. The results are presented in Fig. A8 in the Appendix. Similar to the state decoding, the use of the whole grid caused a significant decoding improvement across all band combinations (sign test, $p = 3.05 \times 10^{-5}$ for Subjects 1 and 2, and $p = 3.70 \times 10^{-3}$ for Subjects 3, 4 and 6). For Subject 4, the improvement was not statistically significant. After averaging over all frequency band combinations, the relative decoding error changes of −42.4%, −33.8%, −8.5%, −32.4%, −11.0%, and −23.0%, were obtained for Subjects 1–6, respectively. Similar results were obtained by comparing the minimum errors (best performances), where the whole-grid decoding led to relative decoding error changes of −56.0%, −44.2%, −7.2%, −41.1%, +2.9%, and −37.5%, for Subjects 1–6, respectively. Thus, even though the inclusion of non-M1 areas generally reduced the decoding error, the advantage of HD over standard grids was preserved. This can be seen by comparing $\overline{\text{S}}$ and $\overline{\text{HD}}$ in Fig. A8, which demonstrates that HD grids reduced the average decoding error from 29.8% to 18.4%. This represents a relative error reduction of 38.3%, and is somewhat inferior to the improvement observed in the M1 decoding (cf. Section 3.3.1). Likewise, by averaging the best performances over subjects, HD grids reduced the decoding error from

20.9% to 8.8%. This corresponds to a relative error reduction of 57.9%, and is slightly inferior to the error reduction seen in M1 (cf. Section 3.3.4). This discrepancy in the error reduction between M1 and whole-grid decoding could be explained by standard grids covering much larger brain areas (Fig. 2), and consequently benefiting more by including information outside of M1.

3.3.6 Confusion Matrices—A further insight into the decoding accuracy based on standard and HD ECoG signals can be obtained by analyzing the confusion matrices (see Fig. 7). For both grid types, shoulder flexion/extension was the movement decoded with the highest accuracy. On the other hand, the movements decoded with the lowest accuracy were pronation/supination for standard and wrist flexion/extension for HD grids. Generally, HD grids yielded a more uniform decoding accuracies ranging from to 78.0% to 96.5%, whereas those based on standard grids ranged between 36.6% and 77.9%. In addition, for both grid types, pincer grasp/release was rarely confused with either shoulder flexion/extension or shoulder rotation movements. Conversely, shoulder movements were rarely confused with pincer grasp/release. This is consistent with the classic somatotopic arrangement of M1, where the representations of finger and shoulder movements are respectively at the lateral and medial extremes of the M1 arm motor area [10]. Another observation consistent with the "motor homunculus" organization of M1 is that a pair of DOFs with adjacent representation areas tended to be more confused by the decoder. Examples include: wrist flexion/extension confused with either pronation/supination (both grid types) or pincer grasp/release (standard grid); pronation/supination confused with either wrist flexion/extension or elbow flexion/extension (both grid types); elbow flexion/extension confused with shoulder rotation; and shoulder rotation confused with elbow flexion/extension.

4 Discussion

Power modulation analysis confirmed the general alignment of anatomical and functional motor cortices, suggesting that both standard and HD grids were properly placed over the intended M1 arm areas. This further suggests that the advantages of HD grids were likely due to their higher density rather than a more favorable placement. In addition, the higher CI values of the HD grids (cf. Table 2) indicate that their electrodes recorded signals of higher fidelity. This was presumably caused by the smaller electrode diameter of the HD grids (2 mm vs. 4 mm), although other factors may have contributed. Finally, note that pronounced high-γ power modulation in S1 (Figs. 3 and 4, Figs. A1–A4) could be explained by sensory feedback such as proprioception. This was confirmed by performing the time-domain analysis of the high-γ power, which showed that S1 signals generally lagged behind their M1 counterparts, and that these latencies were within a physiologically plausible range (Section 3.1).

By comparing the average state decoding performances of standard and HD grids, it can be concluded that HD grids yielded a 46.7% relative error reduction (Section 3.2.1). An even higher performance gain was observed in terms of the peak decoding accuracy, where HD grids led to a relative error reduction of 69.4% (Section 3.2.4). Conversely, spatial sub-sampling of the HD grids resulted in a significant reduction of the decoding accuracy, thereby yielding performances that were comparable, albeit superior, to those of standard

grids. While not statistically significant, the slight performance advantage of the spatially sub-sampled HD grids over their standard grid counterparts could be explained by their marginally smaller inter-electrode distance (8 mm vs. 10 mm). The higher signal fidelity of the HD electrodes (represented by higher CI values) could be another contributing factor. Control analysis also demonstrated that the decoding advantage of HD grids was likely caused by higher electrode density and signal fidelity, and not by having a larger number of M1 channels. In addition, the inclusion of all available electrodes reduced the decoding error for both grid types; however, the relative advantage of HD over standard grids was retained.

The advantage of the HD over standard grids was also observed in movement decoding. Namely, the HD grids yielded a 43.8% (64.0%) relative decrease in the average (minimum) decoding error, respectively. Upon spatial sub-sampling, the decoding errors increased while approaching those achieved with standard ECoG signals. Similar to the state decoder, the marginally higher decoding accuracy achieved with the spatially sub-sampled HD grids could be explained by factors such as smaller inter-electrode distance and higher signal fidelity. Control analysis also showed that the decoding performance of HD grids could be replicated by selecting a subset of 14 M1 channels, thus matching the average number of M1 channels of standard grids. This, in turn, confirmed that the advantage of HD grids was due to higher electrode density and signal fidelity, and not due to featuring a larger number of M1 channels. Finally, the inclusion of non-M1 areas reduced the decoding error for both grid types. However, HD grids still outperformed standard grids by a significant margin.

The analysis of confusion matrices revealed that the HD grids yielded not only higher performances, but also more uniform decoding results across the movement types. In addition, for both grid types, movements were on average less confused by the classifier, if their cortical representations were on the opposite ends of the arm M1 area. Conversely, movements with adjacent cortical representation areas tended to get more easily confused. The fact that the high-γ band power was the most informative single feature for upper extremity movement classification is consistent with prior reports [24, 25, 27]. Unlike the μ and β bands, which are broadly distributed and spatially non-specific, the high-γ band is known to have a more spatially specific distribution [26]. Consequently, this band, particularly as detected by the HD grids, facilitated better distinction of different upper extremity movements.

As mentioned in Section 1, there have only been few prior reports concerned with the decoding of six elementary upper extremity movements from ECoG signals [9, 11]. Therefore, the results from Section 3.2 and Section 3.3 can only be indirectly compared to those reported in the literature (see Table 5). Since decoding was not restricted to M1 in many of these prior reports, the present study was characterized by the whole-grid decoding errors in order to make the comparison meaningful. Also note that prior results were often achieved with the decoder parameters optimized on a per subject or per task basis. Nevertheless, the decoding performances in the present study, especially those achieved with HD grids, compare favorably to those reported in prior studies.

While standard grids yielded decoding performances significantly above the chance level, these classification errors are too high for practical applications. Note that the combined

minimum error of their state (8.5%) and movement (33.1%) decoders is even higher (38.8%), which would translate into poor control of an upper extremity prosthesis and would likely frustrate the operator. Such a modest decoding resolution of standard grids is caused by a large overlap in the representation of the six movement types (cf. Figs. 3, A1 and A2). The >4-fold increase in electrode density and smaller electrode diameter of HD grids have contributed to a reduction of this overlap (cf. Figs. 4, A3 and A4). Consequently, the decoding accuracy achieved with HD grids was greatly improved, though the best misclassification rates were still non-negligible (2.6% for state and 11.9% for movement). These decoding errors could potentially be further reduced by utilizing functional MRI guidance for a more accurate grid placement, as recently demonstrated in [19]. Extraction of source-level features [42, 43], with the goal of further disentangling the representation of elementary upper extremity movements, may be another approach.

5 Conclusion

This article quantified the ability to decode the state and type of elementary arm movements based on standard and HD ECoG signals, for the purpose of operating a BCI upper extremity prosthesis. It was found that the performances of the state and movement decoders were far superior when signals from HD grids were used instead of their standard grid counterparts. Future work will focus on a further reduction of the decoding error, possibly by employing source-level features. It will also address the decoding of movement trajectories, or the direction of movements.

Acknowledgments

The authors would like to thank Angelica Nguyen and Christel Jean for their assistance in setting up the experiments. This study was supported by the National Science Foundation (Award #1134575).

Appendix

Figs. A1, A2, A3 and A4 show the distribution of the CI for Subjects 2, 3, 4 and 6, respectively. Note that Subjects 2 and 3 were implanted with standard grids, while Subjects 4 and 5 had HD grids. For Subjects 1 and 5, see Figs. 3 and 4 in the main text.

Fig. A5 shows the spectrogram corresponding to pincer grasp/release of Subject 6. The ECoG signals were selected from channel 54, which was an M1 channel with the highest CI value for this movement type (see Fig. A4). The spectrogram was calculated by dividing the ECoG time series into 2-s-long windows with 95% overlap. Short-time Fourier Transform was performed on each window by running the FFT. The PSDs were then log-transformed. Finally, the spectrogram image was smoothed by a 2s×4Hz boxcar window to enhance the appearance.

The time courses of P_γ for the most salient M1 and S1 channels are shown in Fig. A6. As explained in Section 2.3, the traces were averaged over the four idle-to-move transition periods (see Fig. 1). For each type of movement, the results were also averaged over subjects in order to further reduce the noise. At the onset of movement, the values of P_γ from M1 were higher than their S1 counterparts. This suggests a faster build-up of the high-γ power

in M1 than in S1, which was corroborated by calculating the lead/lag times of P_γ for the most salient M1 and S1 channels. The lead/lag time with respect to the movement onset was defined as the time point at which the P_γ trace intersects the 3-MAD line. The exception was the shoulder rotation movement, for which there was no intersection between motor P_γ and the 3-MAD line. In this case, the lead/lag times were calculated as the instances of local minima to the left of the origin. The lead/lag times are summarized in Table A1. For standard grids, P_γ from the M1 electrodes tended to precede their S1 counterparts by ~86 ms, whereas for HD grids, this difference was 38 ms. The smaller value for HD grids likely represents a more reliable estimate due to their superior signal-to-noise ratio, as seen in Fig. A6.

Fig. A7 is the equivalent of Fig. 5 (in main text), with decoding based on all available electrodes. Note that the inclusion of non-M1 areas (most notably S1) resulted in a significant reduction of the state decoding error.

Fig. A8 is the equivalent of Fig. 6 (in main text), with the results obtained by utilizing all available electrodes for decoding. Note that the inclusion of non-M1 areas resulted in a significant reduction of the movement decoding error.

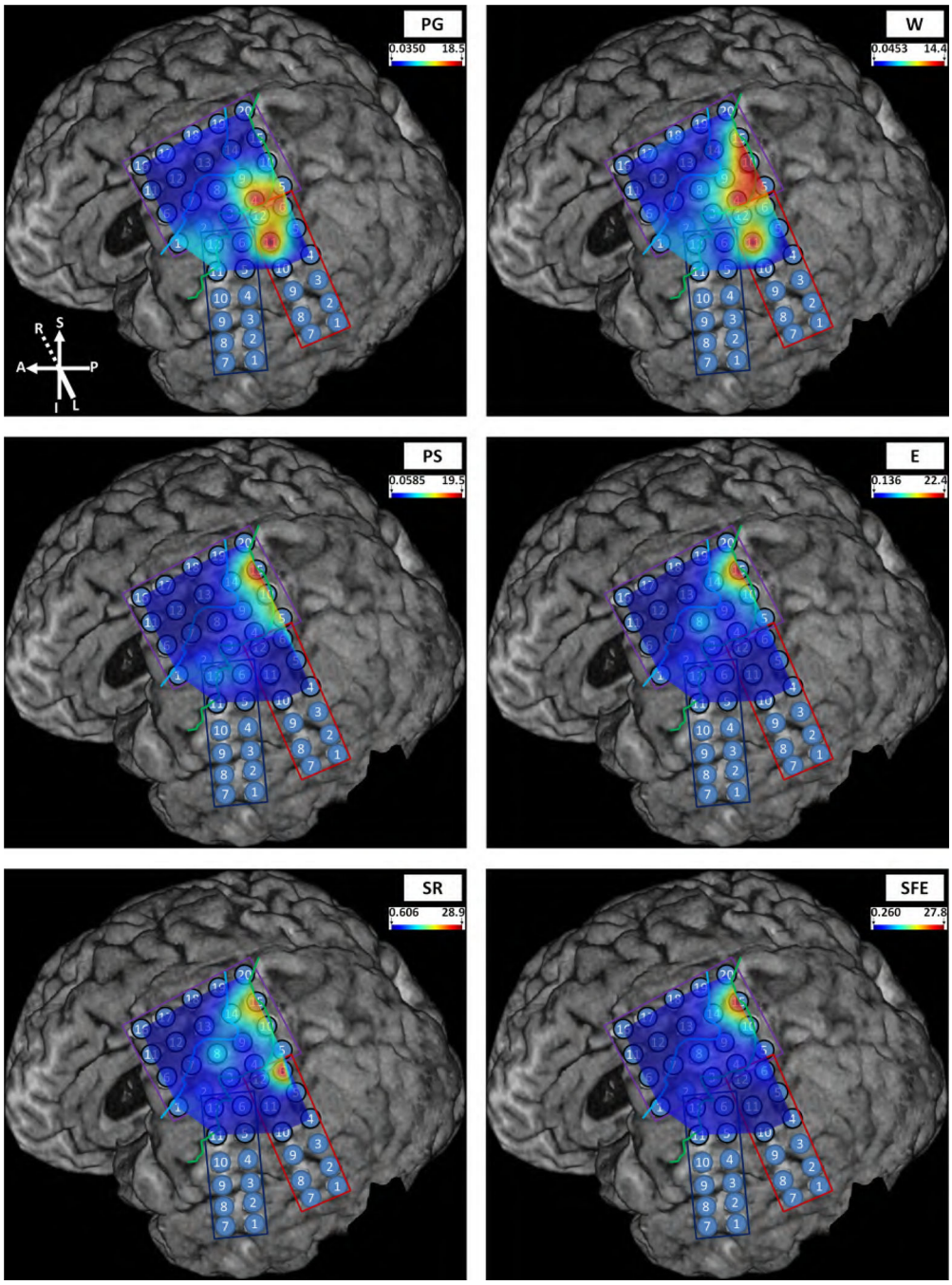

Figure A1:
The CI map for different movement types for Subject 2 (standard grid). The CI was calculated according to (3).

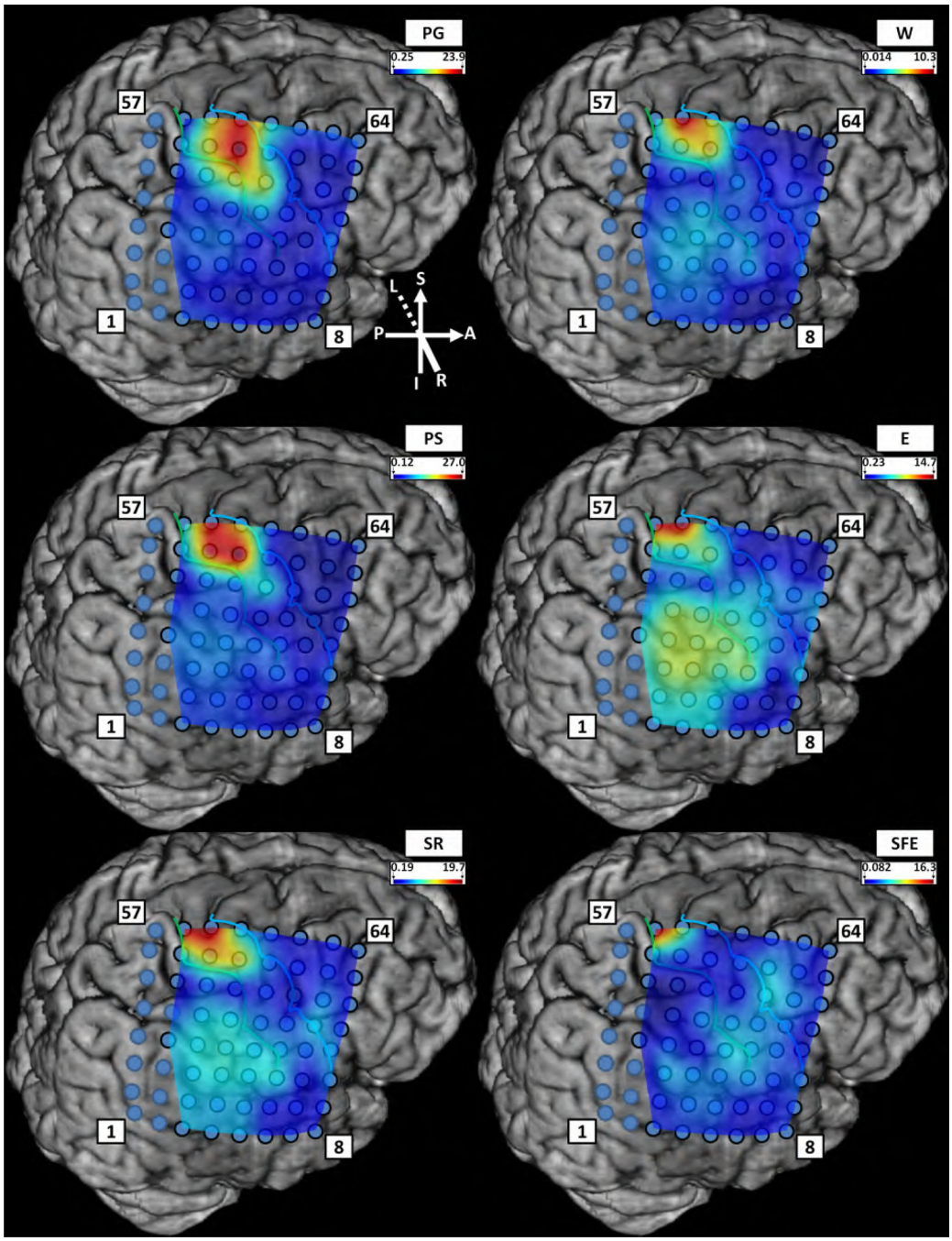

Figure A2:
An equivalent figure for Subject 3 (standard grid).

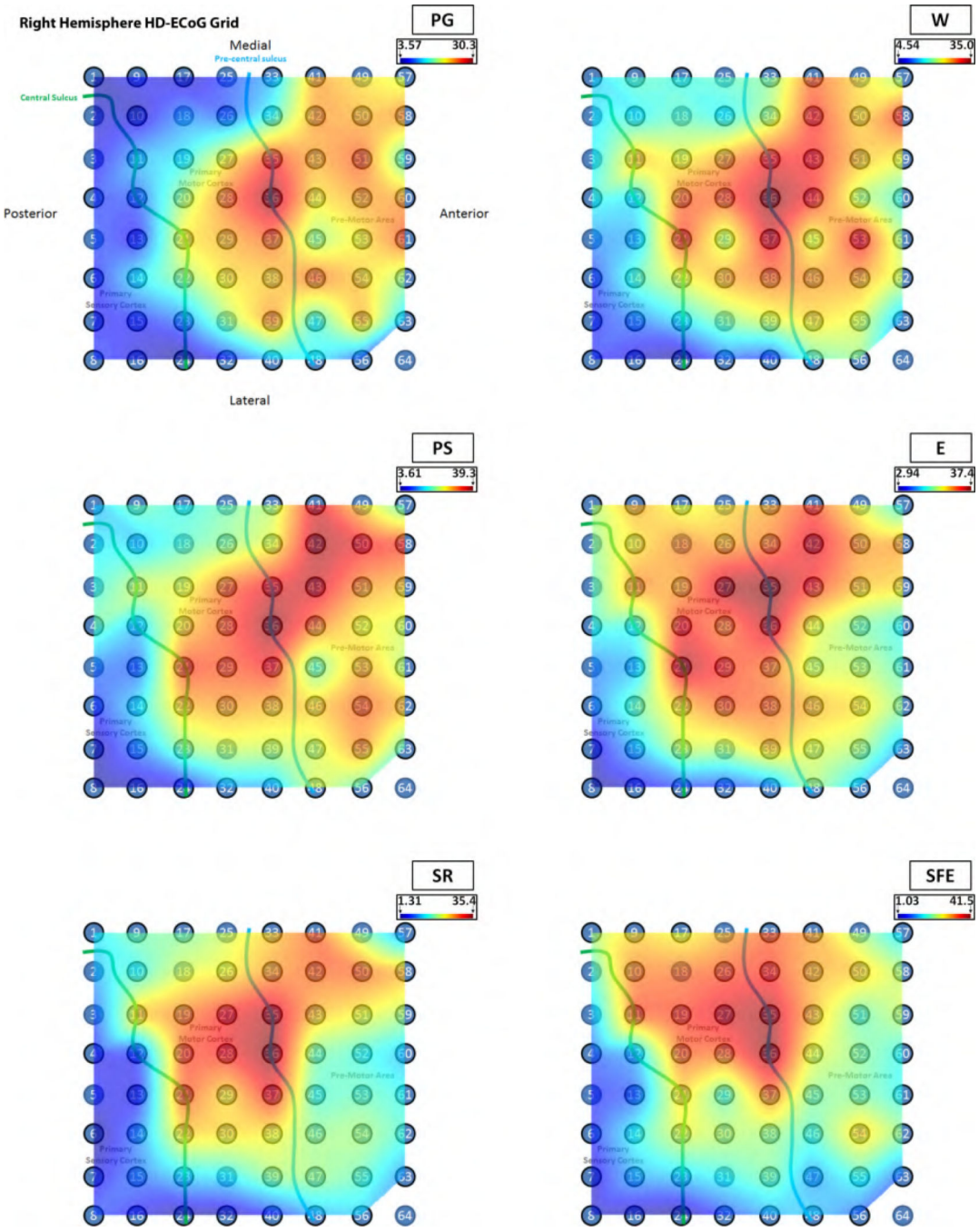

Figure A3:
An equivalent figure for Subject 4 (HD grid).

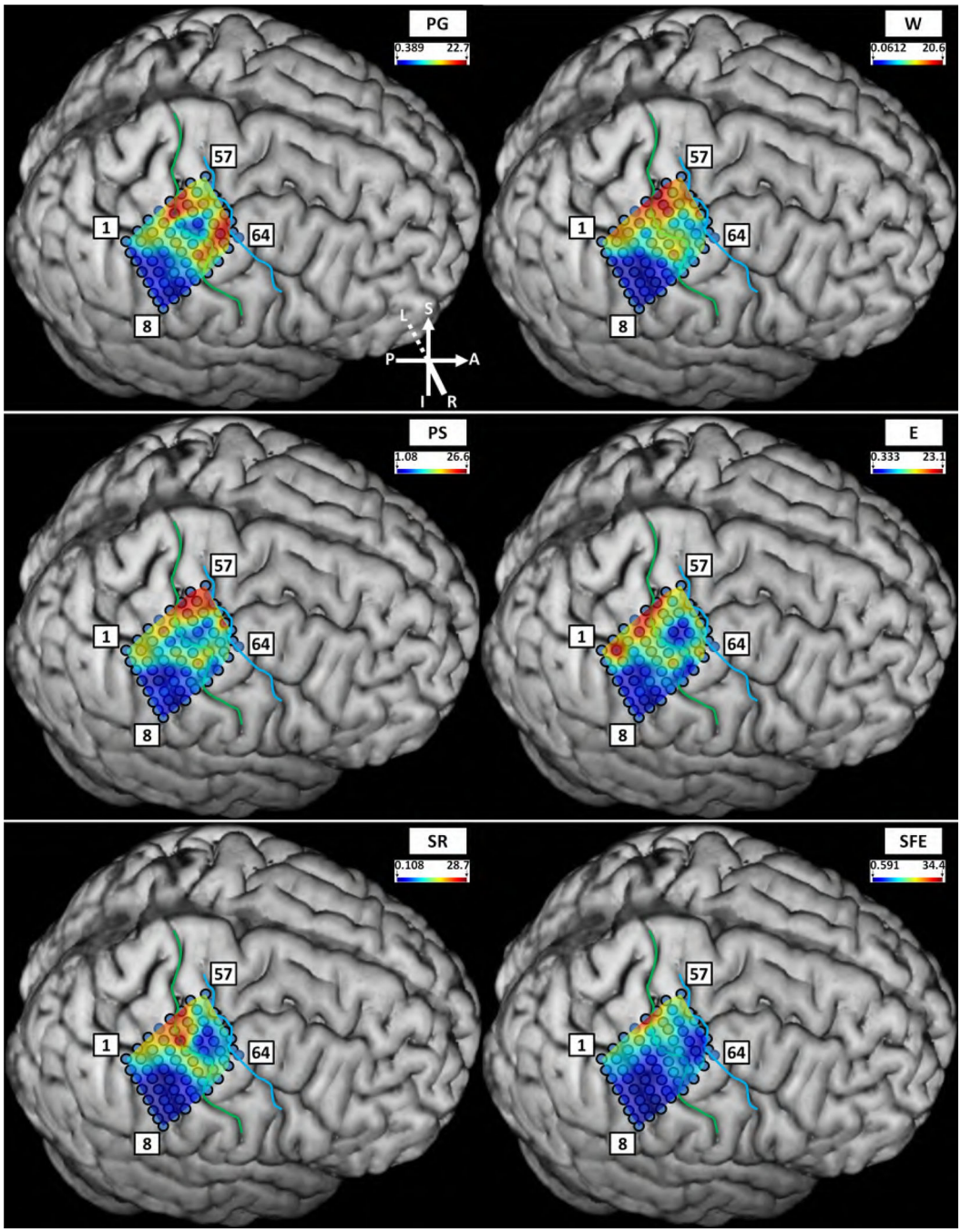

Figure A4:
An equivalent figure for Subject 6 (HD grid).

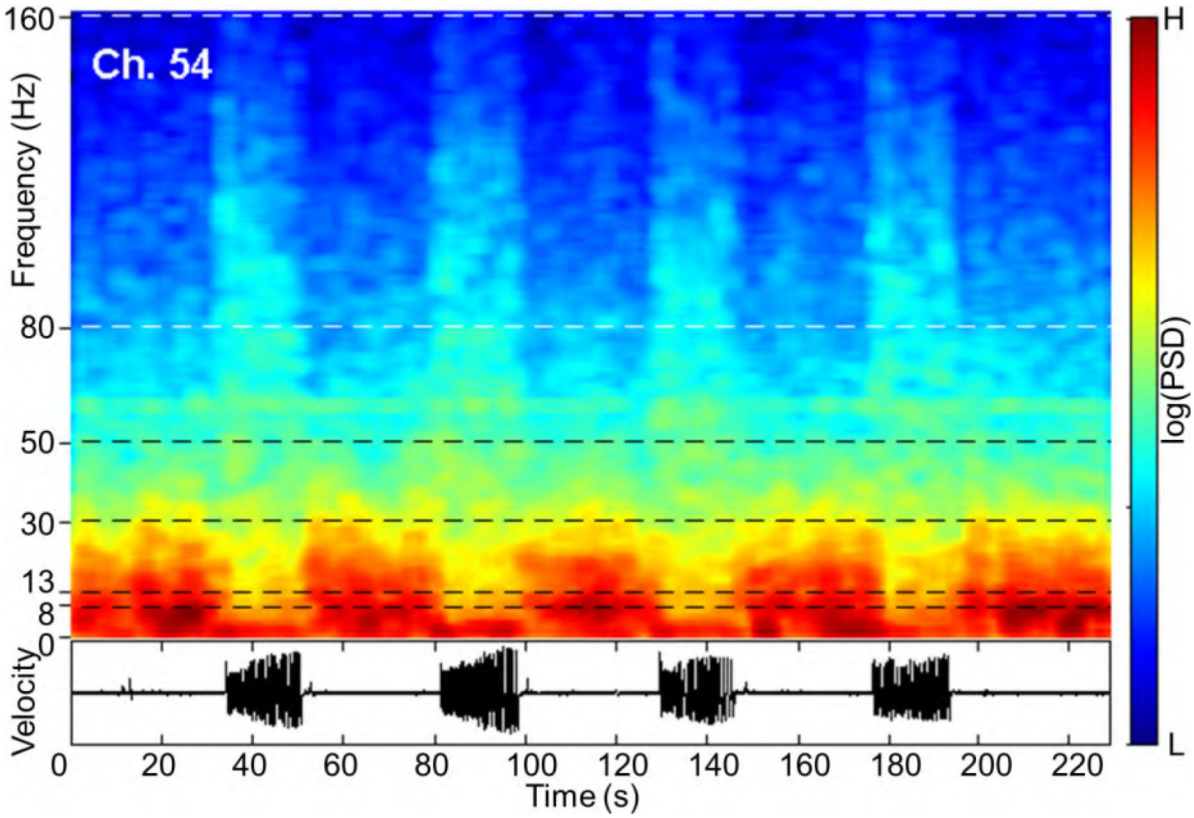

Figure A5:

A spectrogram showing the power modulation in response to the idling and repetitive pincer grasp/release for Subject 6. The data correspond to channel 54, which was the most functionally-relevant M1 channel for this type of movement (see Fig. A4). The dashed horizontal lines mark the upper and lower bounds for the α, β, low-γ and high-γ frequency bands. The bottom plot shows the finger velocity trace obtained by differentiating electrogoniometry measurements.

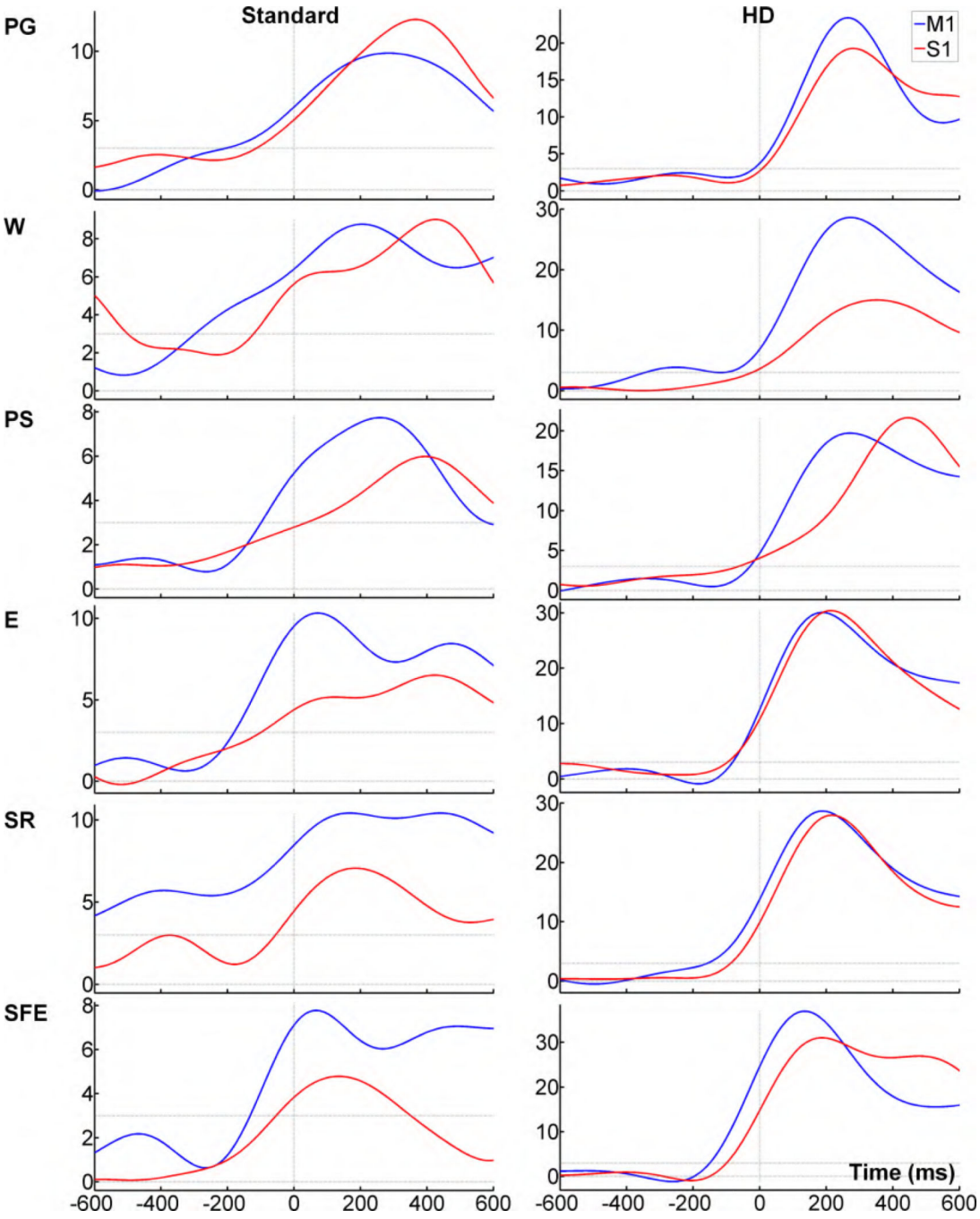

Figure A6:

Time courses of P_γ for the most relevant M1 (motor) and S1 (sensory) channels for each type of elementary movement. The results represent averages across subjects with standard (Subjects 1–3) and HD (Subjects 4–6) grids. The 0-ms time point marks the onset of the movement, as determined from the motion sensor data (velocity>5°/s). Note that the initiation of movement is likely to happen earlier due the threshold-induced delay. The dashed horizontal lines represent the 0-median and 3-MAD levels.

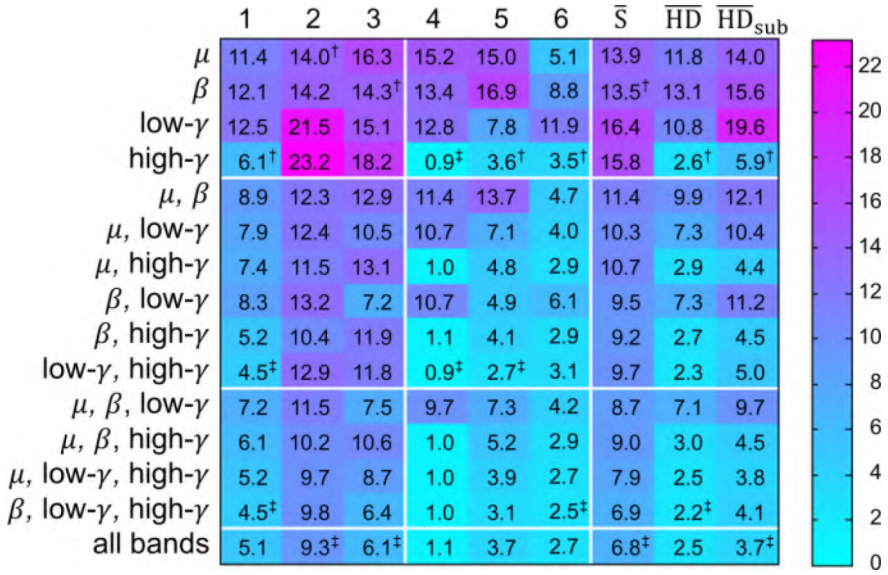

Figure A7:

The state decoding error (%) using all available electrodes in the grid. Compare to Fig. 5 in the main text.

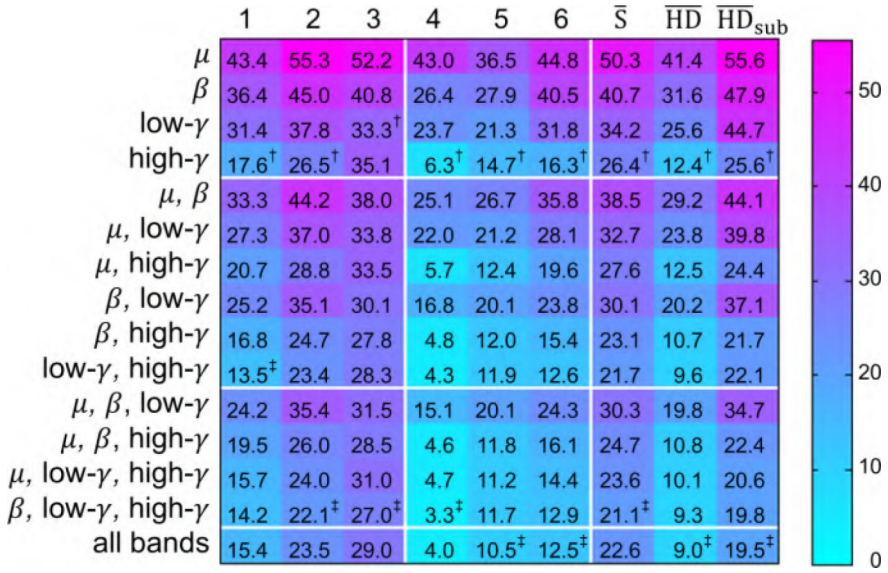

Figure A8:
The movement decoding error (%) using all available electrodes in the grid. Compare to Fig. 6 in the main text.

Table A1:

The distribution of P_γ lead/lag times (in ms) with respect to the onset of movement for M1 and S1 channels. The last column shows the time difference between M1 and S1 channels, with negative values indicating that motor signals precede sensory signals. The last rows give the median values over all movements for both grid types (S-standard, HD high-density).

Grid	Movement	M1	S1	M1 - S1
S	PG	−207	−114	−93
	W	−297	−122	−176
	PS	−99	37	−136
	E	−180	−100	−81
	SR	−252	−180	−71
	SFE	−132	−54	−78
	Median	−193.5	−107.0	−86.5
HD	PG	−18	8	−26
	W	−117	−23	−94
	PS	−29	−64	35
	E	−82	−97	15
	SR	−157	−87	−70
	SFE	−150	−100	−50
	Median	−99.5	−75.5	−38.0

References

[1]. Kubánek J, Miller KJ, Ojemann JG, Wolpaw JR, Schalk G. Decoding flexion of individual fingers using electrocorticographic signals in humans. J Neural Eng. 2009;6(6):66001.

[2]. Wang Z, Ji Q, Miller KJ, Schalk G. Prior knowledge improves decoding of finger flexion from electrocorticographic signals. Front Neurosci. 2011;5:127. [PubMed: 22144944]

[3]. Liang N, Bougrain L. Decoding finger flexion from band-specific ECoG signals in humans. Front Neurosci. 2012;6:91. [PubMed: 22754496]

[4]. Yanagisawa T, Hirata M, Saitoh Y, Kishima H, Matsushita K, Goto T, et al. Electrocorticographic control of a prosthetic arm in paralyzed patients. Ann Neurol. 2012;71(3):353–361. [PubMed: 22052728]

[5]. Wang Z, Gunduz A, Brunner P, Ritaccio AL, Ji Q, Schalk G. Decoding onset and direction of movements using electrocorticographic (ECoG) signals in humans. Front Neuroeng. 2012;5:15. [PubMed: 22891058]

[6]. Chin CM, Popovic MR, Thrasher A, Cameron T, Lozano A, Chen R. Identification of arm movements using correlation of electrocorticographic spectral components and kinematic recordings. J Neural Eng. 2007;4(2):146–158. [PubMed: 17409488]

[7]. Granger CV, Hamilton BB, Linacre JM, Heinemann AW, Wright BD. Performance profiles of the functional independence measure. Am J Phys Med Rehabil. 1993 4;72(2):84–89. [PubMed: 8476548]

[8]. Romilly DP, Anglin C, Gosine RG, Hershler C, Raschke SU. A functional task analysis and motion simulation for the development of a powered upper-limb orthosis. IEEE T Reh Eng. 1994;2(3):119–129.

[9]. Wang PT. King CE. Schombs A. Lin JJ. Sazgar M. Hsu FPK. Shaw SJ. Millett D. Liu CY. Chui LA. Nenadic Z. Do AH. Electrocorticogram encoding of upper extremity movement trajectories; Proc. 6th Ann. Int. IEEE EMBS Conf. Neural Eng.; 2013. 1429–1432.

[10]. Penfield W, Boldrey E. Somatic motor and sensory representation in the cerebral cortex of man as studied by electrical stimulation. Brain. 1937;60(4):389–443.

[11]. Do AH, Wang PT, King CE, Schombs A, Lin JJ, Sazgar M, Hsu FPK, Shaw SJ, Millett DE, Liu CY, Szymanska AA, Chui LA, Nenadic Z. Sensitivity and specificity of upper extremity movements decoded from electrocorticogram. In: Proc. 35th Ann. Int. Conf. IEEE EMBS; 2013 p. 5618–5621.

[12]. Van Gompel JJ, Stead SM, Giannini C, Meyer FB, Marsh WR, Fountain T, et al. Phase I trial: safety and feasibility of intracranial electroencephalography using hybrid subdural electrodes containing macro-and microelectrode arrays. Neurosurgical Focus. 2008;25(3):E23. [PubMed: 18759625]

[13]. Baker J, Bishop W, Kellis S, Levy T, House P Greger B. Multi-scale recordings for neuroprosthetic control of finger movements. In: Proc. 31st Ann. Int. Conf. IEEE EMBS; 2009 p. 4573–4577.

[14]. Leuthardt EC, Freudenberg Z, Bundy D, Roland J. Microscale recording from human motor cortex: implications for minimally invasive electrocorticographic brain-computer interfaces. Neurosurg Focus. 2009;27(1):E10.

[15]. Kellis SS, House PA, Thomson KE, Brown R, Greger B. Human neocortical electrical activity recorded on nonpenetrating microwire arrays: applicability for neuroprostheses. Neurosurg Focus. 2009;27(1):E9.

[16]. Scherer R, Zanos SP Miller KJ, Rao RP Ojemann JG. Classification of contralateral and ipsilateral finger movements for electrocorticographic brain-computer interfaces. Neurosurg Focus. 2009;27(1):E12.

[17]. Wang W, Degenhart AD, Collinger JL, Vinjamuri R, Sudre GP Adelson PD, et al. Human motor cortical activity recorded with Micro-ECoG electrodes, during individual finger movements. In: Proc. 31st Ann. Int. Conf IEEE EMBS; 2009 p. 586–589.

[18]. Flint RD, Wang PT, Wright ZA, King CE, Krucoff MO, Schuele SU, et al. Extracting kinetic information from human motor cortical signals. Neuroimage. 2014 11;101:695–703. [PubMed: 25094020]

[19]. Wang W, Collinger JL, Degenhart AD, Tyler-Kabara EC, Schwartz AB, Moran DW, et al. An electrocorticographic brain interface in an individual with tetraplegia. PLoS ONE. 2013;8(2):e55344. [PubMed: 23405137]

[20]. Wang PT, King CE, Do AH, Nenadic Z. A durable, low-cost electrogoniometer for dynamic measurement of joint trajectories. Med Eng Phys. 2011;33(5):546–552. [PubMed: 21247789]

[21]. Wang PT, King CE, Shaw SJ, Millett DE, and Liu CY and Chui LA, Nenadic Z, Do AH. A co-registration approach for electrocorticogram electrode localization using post-implantation MRI and CT of the head. In: Proc. 6th Ann. Int. IEEE EMBS Conf. Neural. Eng.; 2013 p. 525–528.

[22]. Hermann B, Seidenberg M, Bell B, Rutecki P Sheth R, Ruggles K, et al. The Neurodevelopmental Impact of Childhood-onset Temporal Lobe Epilepsy on Brain Structure and Function. Epilepsia. 2002;43(9):1062–1071. [PubMed: 12199732]

[23]. Brazdil M, Zákopčan J, Kuba R, Fanfrdlová Z, Rektor I. Atypical hemispheric language dominance in left temporal lobe epilepsy as a result of the reorganization of language functions. Epilepsy & Behavior. 2003;4:414–419. [PubMed: 12899862]

[24]. Crone NE, Miglioretti DL, Gordon B, Lesser RP Functional mapping of human sensorimotor cortex with electrocorticographic spectral analysis II. Event-related synchronization in the gamma band. Brain. 1998;121:2301–2315. [PubMed: 9874481]

[25]. Anderson NR, Blakely T, Schalk G, Leuthardt EC, Moran DW. Electrocorticographic (ECoG) correlates of human arm movements. Exp Brain Res. 2012;223(1):1–10. [PubMed: 23001369]

[26]. Miller KJ, Leuthardt EC, Schalk G, Rao RPN, Anderson NR, Moran DW, et al. Spectral changes in cortical surface potentials during motor movement. J Neurosci. 2007;27(9):2424–2432. [PubMed: 17329441]

[27]. Miller KJ, Zanos S, Fetz EE, den Nijs M, Ojemann JG. Decoupling the cortical power spectrum reveals real-time representation of individual finger movements in humans. J Neurosci. 2009;29(10):3132–3137. [PubMed: 19279250]

[28]. Schalk G, Kubánek J, Miller KJ, Anderson NR, Leuthardt EC, Ojemann JG, et al. Decoding two-dimensional movement trajectories using electrocorticographic signals in humans. J Neural Eng. 2007;4(3):264–275. [PubMed: 17873429]

[29]. Wang PT, King CE, Shaw SJ, Millett DE, and Liu CY and Chui LA, Nenadic Z, Do AH. Electrocorticogram encoding of upper extremity movement duration. In: Proc. 36th Ann. Int. Conf IEEE EMBS; 2014 p. 1243–1246.

[30]. Welch BL. The generalization of “Student’s” problems when several different population variances are involved. Biometrika. 1947;34(1–2):28–35. [PubMed: 20287819]

[31]. Miller KJ, denNijs M, Shenoy P Miller JW, Rao RPN, Ojemann JG. Real-time functional brain mapping using electrocorticography. Neuroimage. 2007;37(2):504–507. [PubMed: 17604183]

[32]. Das K, Nenadic Z. An efficient discriminant-based solution for small sample size problem. Pattern Recogn. 2009;42(5):857–866.

[33]. Das K, Nenadic Z. Approximate information discriminant analysis: A computationally simple heteroscedastic feature extraction technique. Pattern Recogn. 2008;41(5):1548–1557.

[34]. Nenadic Z Information discriminant analysis: Feature extraction with an information-theoretic objective. IEEE T Pattern Anal. 2007;29(8):1394–1407.

[35]. Duda RO, Hart PE, Stork DG. Pattern Classification. Wiley-Interscience; 2001.

[36]. Kohavi R A study of cross-validation and bootstrap for accuracy estimation and model selection. In: Int Joint Conf Art Int; 1995 p. 1137–1145.

[37]. Fukunaga K Introduction to Statistical Pattern Recognition. Academic Press; 1990.

[38]. Hume AL, Cant BR, Shaw NA. Central somatosensory conduction time in comatose patients. Annals of Neurology. 1979;5(4):379–384. [PubMed: 443771]

[39]. Claus D Central motor conduction: Method and normal results. Muscle & Nerve. 1990;13(12): 1125–1132. [PubMed: 2266986]

[40]. Shenoy P. Miller KJ. Ojemann JG. Rao RP. Finger movement classification for an electrocorticographic BCI; Proc 3rd Ann Int IEEE EMBS Conf Neural Eng; IEEE; 2007. 192–195.

[41]. Nenadic Z, Rizzuto DS, Andersen RA, Burdick JW. Advances in cognitive neural prosthesis: Recognition of neural data with an information-theoretic objective In: Dornhege G, d R Millán J,

Hinterberger T, McFarland DJ, Müller KR, editors. Toward Brain-Computer Interfacing. The MIT Press; 2007 p. 175–190.

[42]. Kavanagk RN, Darcey TM, Lehmann D, Fender DH. Evaluation of Methods for Three-Dimensional Localization of Electrical Sources in the Human Brain. IEEE Transactions on Biomedical Engineering. 1978;BME-25(5):421–429.

[43]. Baillet S, Mosher JC, Leahy RM. Electromagnetic brain mapping. Signal Processing Magazine, IEEE. 2001;18(6):14–30.

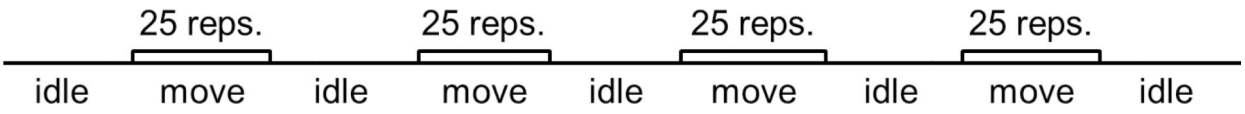

Figure 1:
The timeline of the experimental protocol for each type of elementary movement. Each movement period consisted of 25 movement repetitions, performed in a subject-paced manner.

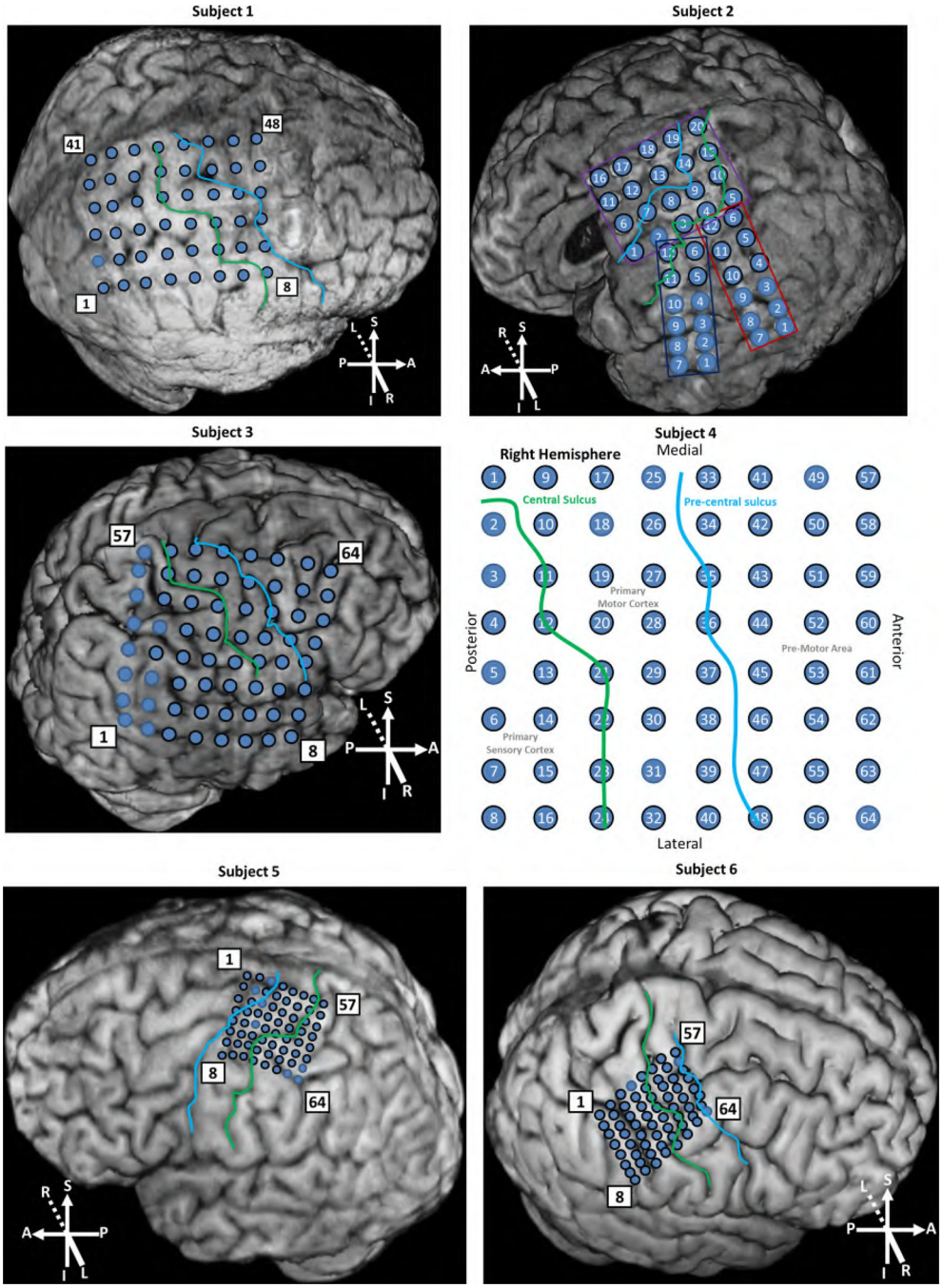

Figure 2:

Grid placement for individual subjects. Subjects 1–3 were implanted with standard and Subjects 4–6 with HD grids (see Table 1). The blue circles represent individual electrodes, and those outlined in black were the ones which were recorded from. The large left frontal cavity in the brain of Subject 2 is due to porencephaly. Orientation legend: A-anterior, P-posterior, S-superior, I-Inferior, L-left, R-right. The pre-central sulcus (cyan); the central sulcus (green).

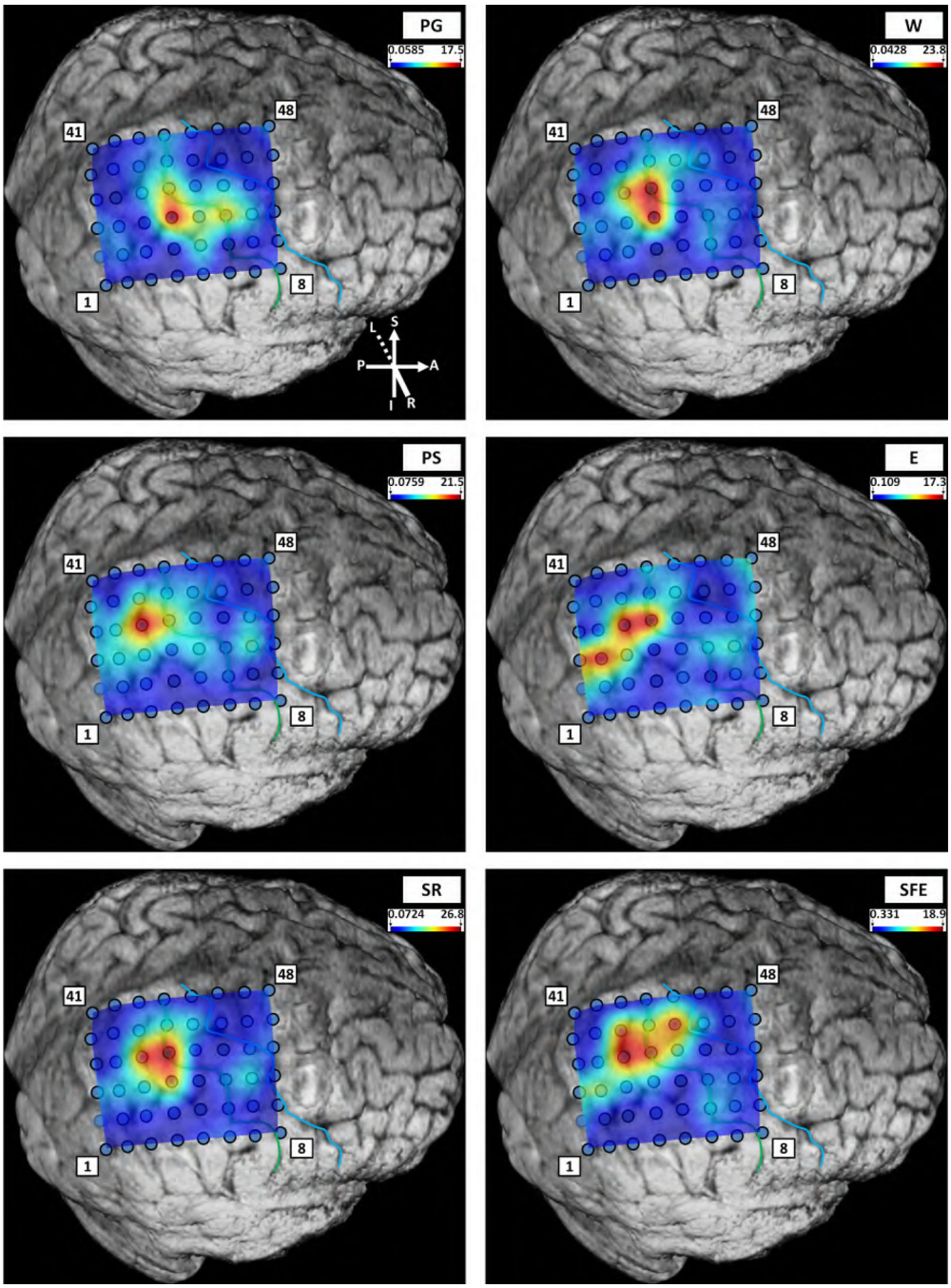

Figure 3:

A representative CI map for all movement types for Subject 1 (standard grid). The red (blue) spots indicate a higher (lower) CI value, respectively. Note that higher CI values correspond to greater high-γ power differences between movement and idling periods (see (3)).

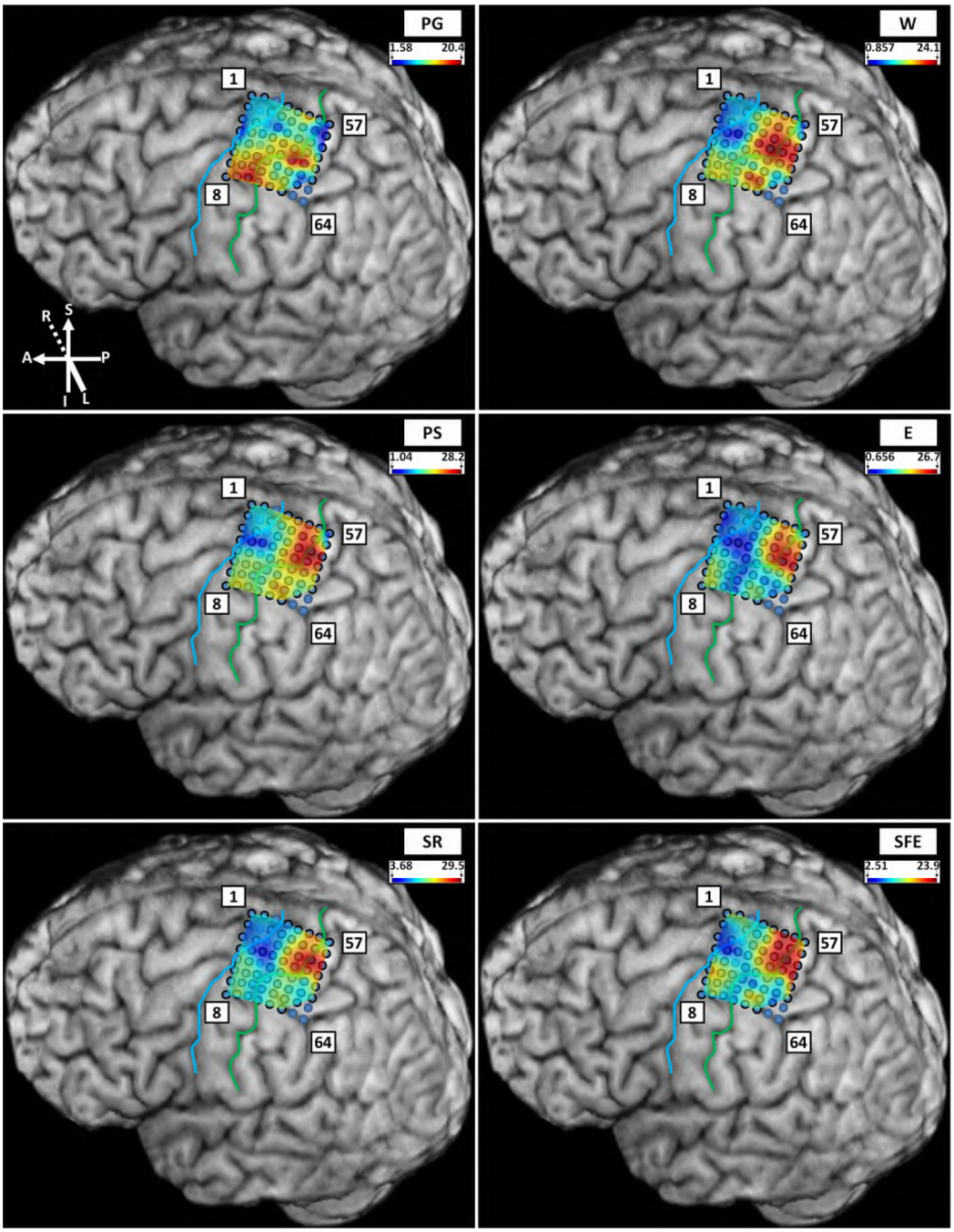

Figure 4:
An equivalent figure for Subject 5 (HD grid).

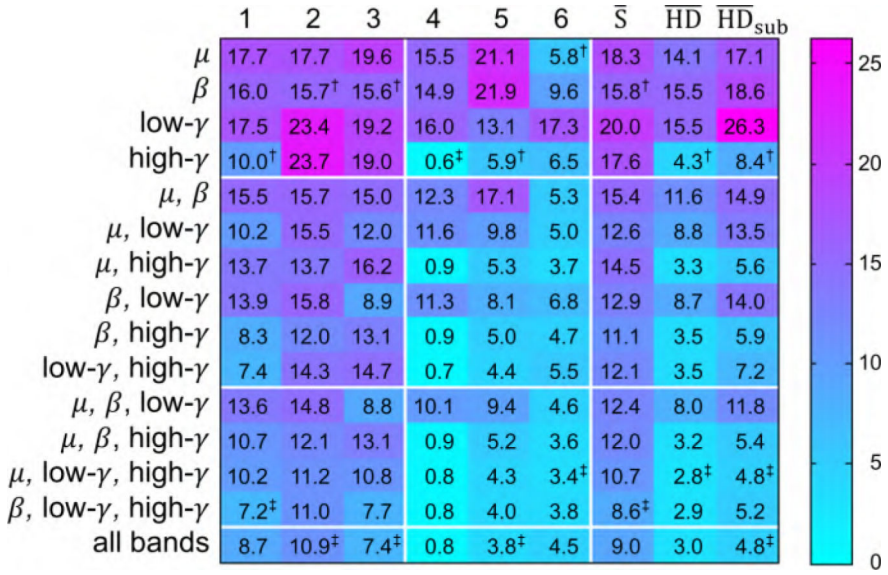

Figure 5:

The decoding error (in %) of the binary classifier (5). The error is color coded for convenience and is broken down by subjects and frequency band combinations († single-band minimum, ‡ overall minimum). $\overline{S}$ and $\overline{HD}$ represent averages over subjects with standard and HD grids, respectively. $\overline{HD}_{sub}$ are averages over subjects with HD grids upon spatial sub-sampling. Note that these results are based on M1 channels only and that the chance-level error is 50.0%.

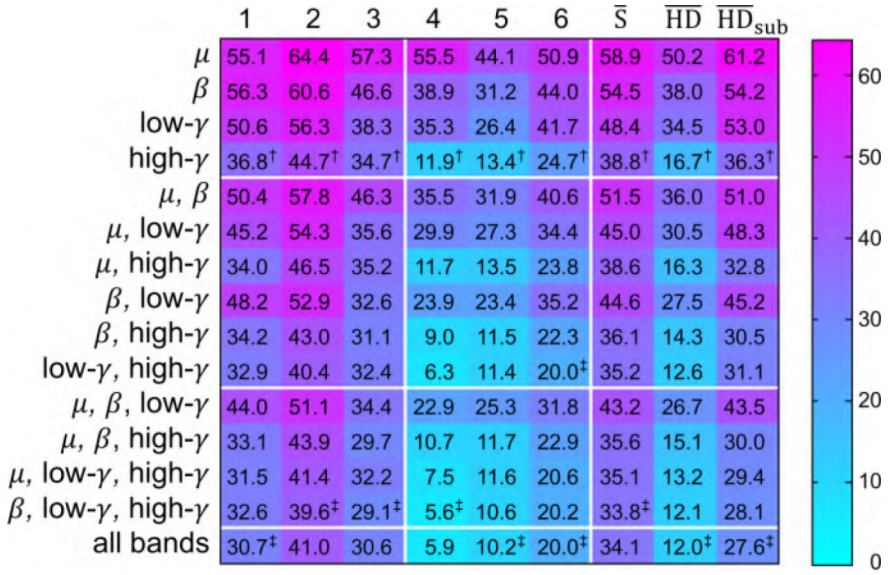

Figure 6:

The decoding error (%) of the six-class classifier (6). The annotation is the same as in Fig. 5. The results are based on M1 channels only. The chance-level error is 83.3%.

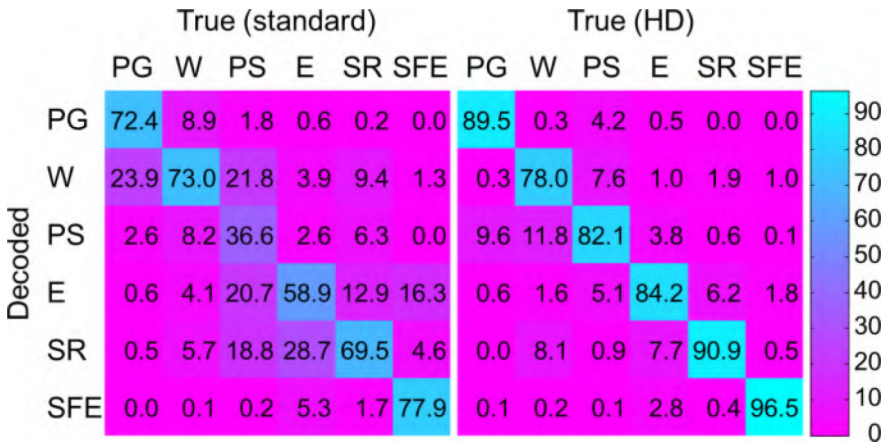

Figure 7:

Confusion matrices averaged over subjects with standard grids (left) and HD grids (right). The element in the ith row and jth column represents the probability (%) that the movement $\mathcal{M}_j$ is decoded as $\mathcal{M}_i$ while utilizing all frequency bands. The probability of correct classification is shown on the diagonal. The column-sum of the matrices is 100%.

Table 1:

Subject demographics together with the side (R-right, L-left) and area of implantation, as well as the grid type (S-standard, HD-high density) and size.

Subject	Age	Gender	Side	Area	Grid	Size
1	27	F	R	Fronto-parietal	S	6×8
2	22	M	L	Frontal Parieto-temporal	S	4×5 2×(2×6)
3	23	F	L	Frontal	S	8×8
4	38	M	R	Fronto-parietal	HD	8×8
5	26	M	L	Fronto-parietal	HD	8×8
6	33	F	R	Fronto-parietal	HD	8×8

Table 2:

The spatial distribution of CIs. N is the total number of recording channels, N_{M1} is the total number of M1 channels, and N_{fr} is the total number of functionally-relevant M1 channels. The CIs were calculated according to (3), and averaged over movement types and channels (non-M1, M1, and functionally-relevant M1).

Subject	N	N_{M1}	N_{fr}	$\overline{CI}_{non-M1}$	$\overline{CI}_{M1}$	$\overline{CI}_{fr}$
1	47	14	3	3.80	5.32	11.10
2	29	11	7	2.58	6.13	7.95
3	52	16	8	3.65	7.03	10.98
Average	42.7	13.7	6.0	3.34	6.16	10.01
4	58	26	5	19.05	22.14	32.55
5	57	31	7	12.24	14.70	19.68
6	60	26	14	7.07	13.22	16.15
Average	58.3	27.7	8.7	12.79	16.69	22.79

Table 3:

The comparison of the decoding errors (%) based on all M1 channels and a subset of 14 channels for subjects with HD grids. The results were obtained using a combination of μ, β, low-γ and high-γ frequency bands.

Subject	4	5	6
All channels	0.8	3.8	4.5
14 channels	0.7	2.8	3.2

Table 4:

The comparison of the decoding errors (%) based on all M1 channels and a subset of 14 channels for subjects with HD grids. The results were obtained using the combination μ, β, low-γ and high-γ frequency bands.

Subject	4	5	6
All channels	5.9	10.2	20.0
14 channels	5.4	8.4	18.0

Table 5:

Comparison of the present study with other ECoG-based decoding studies. The columns specify the decoding task, grid type, the number of subjects (n), the average number of electrodes used (N), chance-level error (%), and the minimum decoding error (%).

Study	Task	Grid	n	N	Chance	Error
[40]	finger movement	S	6	64	80.0	23.0
[41]	direction of arm movement	depth	1	4	50.0	4.9
[41]	behavioral state	depth	1	4	75.0	24.0
[16]	finger movement	S/HD	2	1	50.0	11.1
[1]	finger movement	S	5	58	80.0	19.7
[17]	finger movement	HD	1	16	80.0	27.0
present	movement state	S	3	43	50.0	6.6
present	movement state	HD	3	58	50.0	2.0
present	type of movement	S	3	43	83.3	20.9
present	type of movement	HD	3	58	83.3	8.8